Optical cloaking of macroscopic objects by geometric-phase vortex processing

Mushegh Rafayelyan, Henrik Melkonyan, Arman Tigranyan, Etienne Brasselet

Optical cloaking of macroscopic objects by geometric-phase vortex processing

Mushegh Rafayelyan[1,2], Henrik Melkonyan[2], Arman Tigranyan[2] and Etienne Brasselet[1,*]

[1] Université Bordeaux, CNRS, LOMA, UMR 5798, F-33400 Talence, France
[2] Department of Physics, Yerevan State University, 1 Alex Manoogian, 0025 Yerevan, Armenia

E-mail: etienne.brasselet@u-bordeaux.fr

Abstract

We report on free-space strategy for electromagnetic concealment of three-dimensional macroscopic objects in the optical domain owing to unique energy flow redirection capabilities enabled by optical phase singularities. We propose and implement the generation of a quasi-nodal volume based on optical vortex Fourier processing, which inhibits light scattering from objects placed inside. The proof of concept is made by numerical simulations and the experimental implementation is carried out in the visible domain by using geometric phase vortex phase masks. Optical cloaking demonstration is made by using stainless steel sphere as the object to be concealed. The geometric phase nature of the vortex masks confers polarization independent features to the device and makes it possible to implement in a reflection mode.

Keywords: geometric phase, cloaking, optical vortices

1. Introduction

To see an object using waves, the observer must essentially detect the changes made by the object to the illuminating wave as waver-matter interaction takes place, or detecting the wave emitted by the object itself. Preventing the scattering of a probing wave is a usual option for stealth technologies with the aim at escaping detection from radar in electromagnetism and sonar in acoustics. Concealment management can also consist to absorb the radiation from an emitting object covered by an absorbing material, which is relevant for thermal radiation. The ability of an object to escape attempted observation under irradiation can also be achieved by redirecting the field around the object so that there is no field-object interaction, allowing the object to remain hidden from an observer. Such strategy has been originally proposed in 2006 and relies on specific dielectric and magnetic properties of metamaterials enabling the redirection of the electromagnetic flow around an object embedded in a stealth medium acting as an invisibility cloak, as shown by Leonhardt [1] and by Pendry *et al* [2]. In that case, the effective behavior of the 'cloak + object' is that of free-space, which does not require the cloak to adapt to the object to be concealed, in contrast to earlier attempt [3]. Noteworthy, although the former approach deals with geometrical optics whereas the latter accounts for the Maxwell's equations, both of them basically rely on coordinate transformations [4] and transformation optics is nowadays a standalone research topic [5]. So far, numerous devices to hide objects have been proposed [6–8] and efforts have been paid to the development of cloaking devices that are robust against wavelength, polarization or coherence variations for the probing field [9–18].

In particular, cloaking devices for macroscopic objects that operate in the optical domain arouse interest for applications. Conventional isotropic or anisotropic homogeneous optical elements such as optical lenses [19], calcite crystals [20], or even simple water-filled reservoirs [21] have been shown suitable for concealing macroscopic objects in the visible range. Noticeably, these geometrical optics based approaches do not rely on the fabrication of large-scale devices based on optical

* Author to whom any correspondence should be addressed.

metamaterials requiring nanoscale resolution. It should be noted that the preceding examples of electromagnetic concealment of macroscopic objects that can be described and understood from ray-tracing analysis are not unique to the optical domain. See, for example [22, 23], which report on graded index lensing concealment strategies in the microwave and radio wave domains, respectively, however, with objects whose size is comparable to the wavelength.

Wave-optics cloaking device relying on isotropic refractive optical elements has also been demonstrated by using the nodal line associated with the optical phase singularity of an optical vortex beam as a polarization-independent 1D concealing region [24]. To turn it into a cloaking device, Sun *et al* used a pair of refractive spiral phase plates having opposite topological charges ± 1 and illuminated by a Gaussian laser beam. The first one generates a single-charge on-axis optical vortex beam whose propagation is barely affected when placing a metallic needle with small enough diameter along the propagation axis while the second restores a quasi-Gaussian beam by cancelling the optical phase singularity.

Here, by combining the use of refractive regular optics (standard lenses) with singular geometric-phase optical elements (optical vortex phase masks), we extend the previous use of a point of null intensity in the transverse plane [24] to the use of a nodal surface. This allows considering polarization-independent concealment of three-dimensional (3D) objects. This is made possible by using two cascaded stages of optical vortex Fourier processing, each of them consisting to impart an optical phase singularity to the zero spatial frequency component of the light field. The first stage allows generating a nodal area—a remarkable wave-optics phenomenon introduced in 2005 in the context of high-contrast astronomical imaging [25, 26]—while the second stage restores the illuminating light source. The quasi-nodal volume surrounding the nodal area subsequently behave as a region of space that inhibits light scattering from objects placed inside.

The paper is organized as follows. The section 2 introduces the cloaking device made of an aperture, four lenses and two geometric phase vortex masks. Analytical description of the cloaking region is then given and main figures of merit are discussed. A numerical optical cloaking experiment is presented in section 3 assuming a spherical perfect conductor as the object to conceal. Moreover, the operation principle is explored as a function of its position inside the cloaking region. The section 4 then report on the experimental assessment of the quasi-nodal volume as well as optical cloaking demonstration using a 2 mm diameter stainless steel sphere and the section 5 summarizes the study.

2. Geometric phase optical cloak device

The proposed optical cloaking device is depicted in figure 1(a). It consists of two stages of vortex Fourier processing. Each of them is made of a pair of lenses with focal length f placed at a distance $2f$ from one another. Two phase masks having complex conjugated transfer function $\exp(\pm 2i\phi)$, where ϕ is the polar angle in the cylindrical coordinate system (r,ϕ,z) and z refers to the optical axis of the system, is placed at equal distance from the two lenses. By placing a circular clear aperture with radius R at a distance f before the first lens, a nodal area with radius R is obtained at a distance f from the second lens, which defines the plane $z = 0$, provided that the aperture is illuminated by a plane wave [25, 26]. The second optical vortex Fourier processing stage allows recovering the uniformly illuminated entrance pupil aperture at a $4f$ distance downstream the nodal area. The optical cloaking principle relies on the fact that the nodal area is surrounded by a volume with low-level intensity. This quasi-nodal volume defines the cloaking region, as indicated in figure 1(a).

Quantitatively, the intensity distribution between the two vortex Fourier filters can be obtained from the knowledge of the effect of a thin spherical lens in the paraxial regime, which is mathematically expressed by an integral relationship between the field before and after a lens in free space [27]. In the present case, introducing the normalized transverse and longitudinal coordinates $\tilde{r} = r/R$ and $\tilde{z} = z/f$, and the characteristic diffraction length $\Lambda = f/(kR)$ where $k = 2\pi/\lambda$ is the wavenumber with λ the wavelength, one gets after calculations, for $-1 < \tilde{z} < 1$,

$$I(\tilde{r},\tilde{z}) = \frac{I_0}{2}\frac{\left|\int_0^\infty J_1(\xi)J_2(\xi\tilde{r})\mathrm{e}^{\mathrm{i}\frac{\xi^2}{2}\frac{\Lambda}{R}(1-\tilde{z})}\mathrm{d}\xi\right|^2}{\int_0^\infty\left|\int_0^\infty J_1(\xi)J_2(\xi\tilde{r})\mathrm{e}^{\mathrm{i}\frac{\xi^2}{2}\frac{\Lambda}{R}(1-\tilde{z})}\mathrm{d}\xi\right|^2\tilde{r}\mathrm{d}\tilde{r}}, \quad (1)$$

where I_0 is the uniform optical intensity irradiating the circular aperture and J_n is the Bessel function of the first kind of order n. In the simulations and experiments reported in sections 3 and 4, we use $R = (1.5, 2, 2.5)$ mm, $f = 200$ mm and $\lambda = 632.8$ nm. Also, we use a collimated continuous-wave He–Ne laser beam whose diameter is large enough to consider the aperture as uniformly illuminated. The corresponding intensity distributions calculated from equation (1) for $R = 2$ mm at $\tilde{z} = (-1, -1/2, 0, 1/2, 1)$ are displayed in the panels (c)–(g) of figure 1, respectively. The intensity distribution in the aperture plane at $\tilde{z} = -4$ and the re-images one at $\tilde{z} = 4$ are shown in panels (b) and (h). The cloaking experiments are conducted by placing a camera at $\tilde{z} = 4$, called from now on the observation plane. If the cloaking scheme works, we thus expect to observe a uniformly illuminated disk of radius R with or without an object placed in the cloaking region.

Although the described principle of operation of the proposed cloaking device does not depend on the nature of the two conjugated vortex phase masks, we argue that choosing geometric phase vortex masks based on inhomogeneous half-wave plates offers enhanced performance. A description of their behavior can be found in [25] and can be summarized by the following transformation of an incident circularly polarized light,

$$\mathbf{c}_\sigma \rightarrow \mathbf{c}_{-\sigma}\exp(i2\sigma m\phi), \quad (2)$$

where $\mathbf{c}_\sigma = (\mathbf{x} + i\sigma\mathbf{y})/\sqrt{2}$ is the unit vector describing a circular polarization, $\sigma = \pm 1$ is the helicity of light and $(\mathbf{x}, \mathbf{y}, \mathbf{z})$

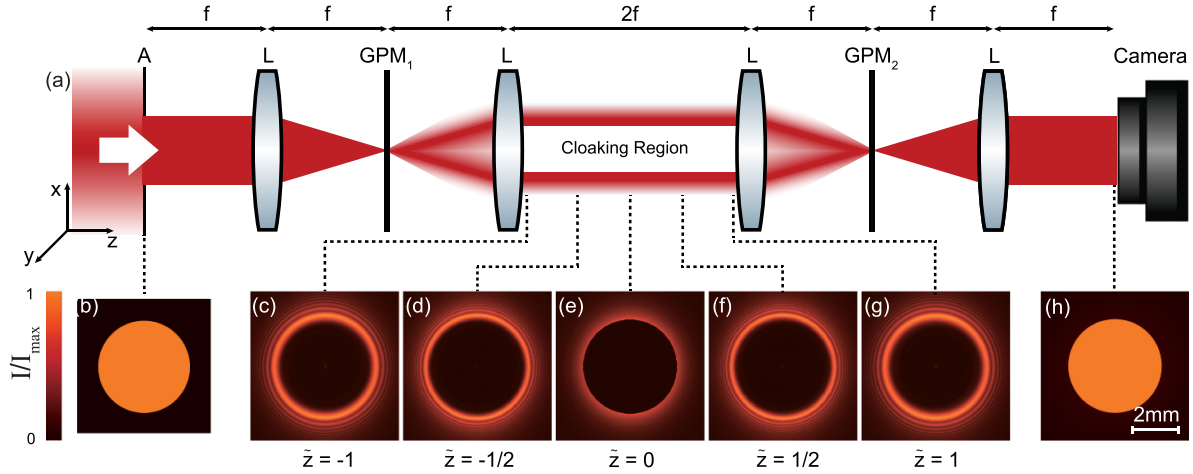

Figure 1. (a) Sketch of the experimental setup for the implementation of geometric phase optical cloaking at the macroscopic scale. A sufficiently expanded continuous-wave collimated laser beam impinges on a circular aperture (A) with radius R. Two $4f$ optical systems made of a pair of lenses with focal length f act on the light field as optical vortex Fourier processors owing to geometric phase masks ($GPM_{1,2}$) placed at $\tilde{z} = \pm 2$, which respectively impart a pure phase singular amplitude profile proportional to $\exp(\pm 2i\phi)$ to the light impinging on it, see text for details. A camera re-images the aperture A at $\tilde{z} = 4$, to which we refer as the observation plane. Panels (b)–(h) show the calculated normalized transverse intensity distributions at various position along the optical axis z, highlighting the quasi-nodal nature of the 3D cloaking region located between the planes $\tilde{z} = \pm 1$.

the orthonormal Cartesian basis and $m = \pm 1$ refers to the azimuthally varying optical axis orientation angle $\psi = m\phi$ in the (x, y) plane for the inhomogeneous half-wave plate. Assuming an input circularly polarized state $\mathbf{c}_\sigma$, the first geometric phase mask is associated with a transfer function $\exp(i2\sigma\phi)$ whereas the circular polarization flipping to the $\mathbf{c}_{-\sigma}$ state makes the second mask having a conjugated transfer function $\exp(-i2\sigma\phi)$. Such a device is therefore inherently polarization insensitive. Indeed, an incident light with an arbitrary polarization state can be described as a superposition of orthogonally polarized states $\mathbf{c}_{\pm 1}$ to which the previous reasoning individually applies. Also, arbitrarily broadband light could be used provided the use a pair of orthogonal achromatic circular polarizers placed, for instance, at $\tilde{z} = -1$ (selection of the $\mathbf{c}_{-\sigma}$ state) and $\tilde{z} = 3$ (selection of the $\mathbf{c}_\sigma$ state). Nevertheless the latter gain in bandwidth comes with an optical throughput trade-off as the circular polarizers will reduce the overall transmitted optical power. Using an achromatic space-variant half-wave plate, whose creation is much more challenging, would waive the latter drawback. Finally, we note that the geometric phase approach allows considering the folding of the setup, by placing a mirror at $\tilde{z} = 0$ (hence using a single geometric phase vortex mask) and adapting the observation to a reflection mode, which cannot be done using a dynamical phase vortex phase mask.

Among the many technological options available for space-variant waveplates such as dielectric nanostructured solid-state media and patterned polymer liquid crystals or liquid crystals, we choose in our experiments the polymer liquid crystal technology (from Beam Engineering) and we select $m = 1$.

3. Numerical simulations

The proposed strategy is first tested numerically by using a spherical perfect conductor as the object to conceal. The simulations are made using free-space Fourier transform propagation in between each optical element of the optical system presented in figure 1 that are treated by complex transfer functions for the amplitude t_X with $X = (A, L, GPM_1, GPM_2)$:

$$t_A(r < R) = 1 \text{ and } t_A(r > R) = 0, \tag{3}$$

$$t_L(r) = \exp\left[-ikr^2/2f\right], \tag{4}$$

$$t_{GPM_1}(\phi) = \exp(i2\sigma\phi), \tag{5}$$

$$t_{GPM_2}(\phi) = \exp(-i2\sigma\phi), \tag{6}$$

where the two last equations refer to a circularly polarized field with helicity σ impinging on the aperture A. In between two transmittance masks the propagation of the field from $\tilde{z}_1$ to $\tilde{z}_2$ is evaluated as

$$E(x, y, z_2) = \mathcal{F}^{-1}\left[\mathcal{F}\left[E(x, y, z_1)\right]\exp[ik_z(z_2 - z_1)]\right], \tag{7}$$

where $\mathcal{F}$ and $\mathcal{F}^{-1}$ refer to fast Fourier and inverse fast Fourier transforms, and $k_z = (k^2 - k_x^2 - k_y^2)^{1/2}$ with $\mathbf{k} = k_x\mathbf{x} + k_y\mathbf{y} + k_z\mathbf{z}$) being the wavevector. Moreover the propagation between the planes $z_o \pm R_o$, where z_o and $R_o = 1$ mm respectively refer to the longitudinal position and the radius of the

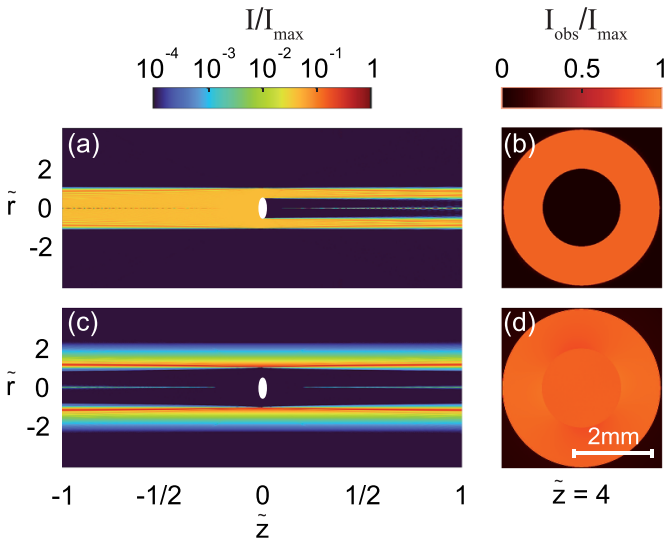

Figure 2. Numerical demonstration of geometric phase optical cloaking. (a), (b) The cloak is deactivated by removing the geometric phase masks. (c), (d) The cloak is activated. In both cases the spherical object to conceal is placed in the center of the cloaking region, at $(r_o, z_o) = (0,0)$. The normalized intensity distributions I/I_{max} inside the cloaking region (panels (a) and (c)) are calculated by using 300 elementary steps along the z axis with 100 of them being dedicated to the object that lies in the range $-R_o < z < R_o$. Note that the sphere (represented in white color) has an elliptical shape in panels (a) and (c) due to the different scaling used for the transverse and longitudinal axes. The normalized intensity distributions I_{obs}/I_{max} in the observation plane at $\tilde{z} = 4$ (panels (b) and (d)) highlight the performance of the cloaking event.

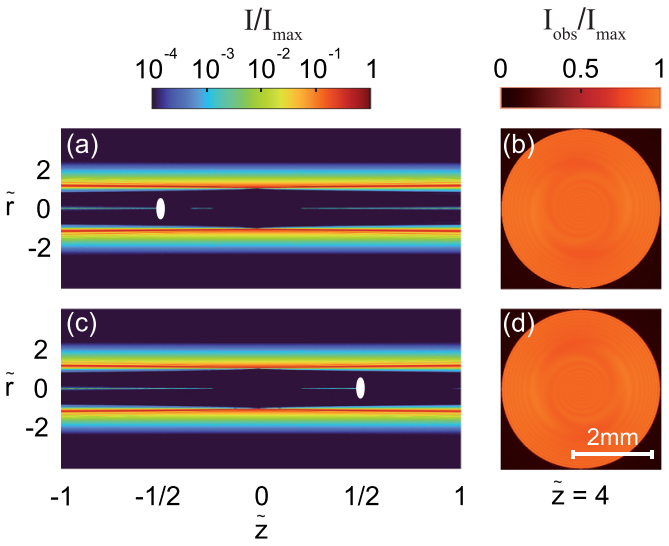

Figure 3. Numerical assessment of the influence of on-axis longitudinal displacement of the object inside the cloaking region. (a), (b) $z_o = -f$. (c), (d) $z_o = f$. The four panels are displayed in a similar manner as in figure 2.

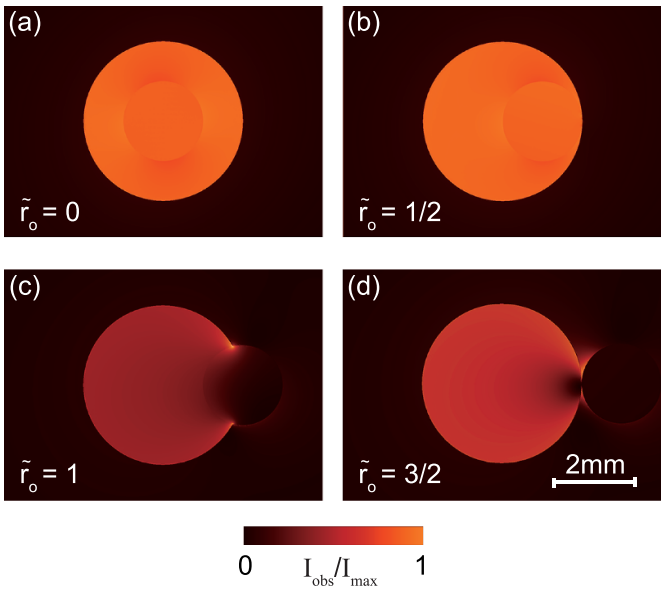

Figure 4. Numerical assessment of the influence of transverse displacement of the object inside the cloaking region at $z_o = 0$ for $\tilde{r}_o = 0$ (a), $\tilde{r}_o = 0.5$ (b), $\tilde{r}_o = 1$ (c) and $\tilde{r}_o = 1.5$ (d).

object to conceal, is carried out by discretizing the spherical object into 100 opaque disks with varying radius that match the spherical envelope of radius R_o.

The optical cloaking demonstration is displayed in figure 2 where the object is placed at $z_o = 0$ with (panels (a) and (b)) and without (panels (c) and (d)) the presence of the geometric phase masks. On the one hand, the panels (a) and (c) show the intensity distributions in the meridional plane of the cloaking region. We choose a logarithmic color bar in order to better appreciate how dark is the quasi-nodal volume when the optical cloak is activated. On the other hand, the panels (b) and (d) show the transverse intensity distributions in the observation plane $\tilde{z} = 4$, which allow appreciating the high level of optical concealment. Indeed, the contrast of the image, defined as $(I_{max} - I_{min})/(I_{max} + I_{min})$ for $r < R$, is reduced from 1 to $\sim$0.05 as the cloak is activated.

Then we evaluate the robustness of the cloaking event with respect to the position (r_o, z_o) of the object inside the cloaking region both along the longitudinal and transverse direction. The results are shown in figures 3 and 4, which respectively correspond to $(r_o, z_o) = (0, \pm f)$ and $([0, 0.5, 1, 1.5], 0)$. On-axis longitudinal displacements barely affect the propagation of light in the cloaking region (figures 3(a) and (c)) and the intensity distribution in the observation plane accordingly remains almost uniform (figures 3(b) and (d)). The optical cloaking is also virtually immune to transverse displacements up to $r_0 = 0.5$ as shown in figures 4(a) and (b) whereas the crossing of the re-imaged aperture A leaves a distinguishable optical footprint, see figures 4(c) and (d).

4. Experimental implementation

The preceding proof of principle analysis is validated experimentally using the same parameters for the optical system, see section 2. The structure of the cloaking region is retrieved by direct imaging, scanning a camera along the z axis. A

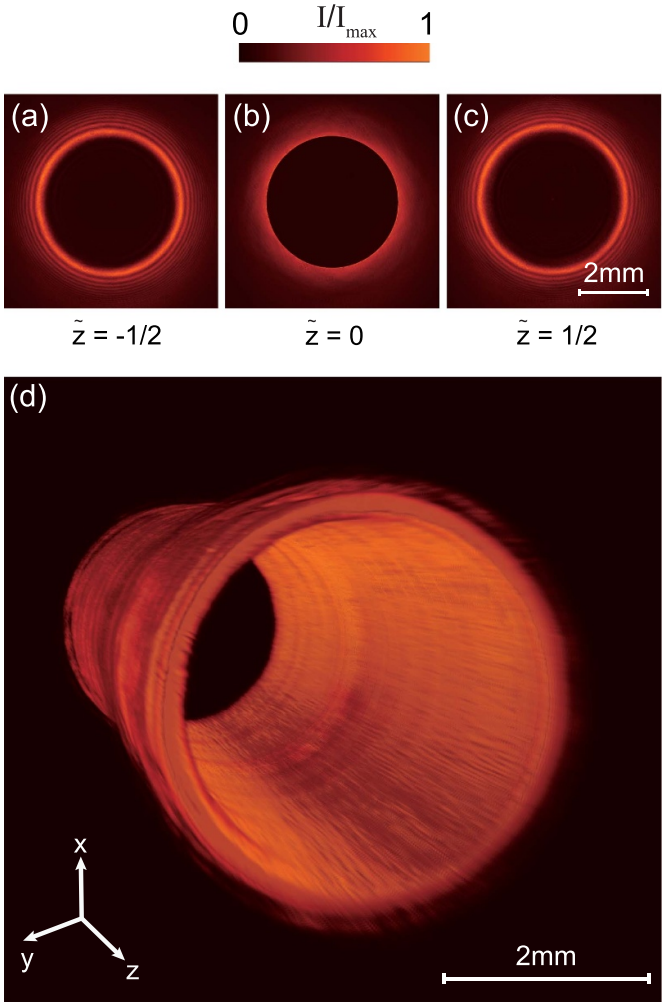

Figure 5. (a)–(c) Experimental measurement of the transverse intensity profiles at different positions inside the cloaking region, $\tilde{z} = (-0.5, 0, 0.5)$, in the absence of the object. (d) Experimental 3D construction of the tube-like intensity boundaries that define the cloaking region based on a collection of 31 equidistant transverse intensity profiles in the range $-0.94 < \tilde{z} < 0.94$.

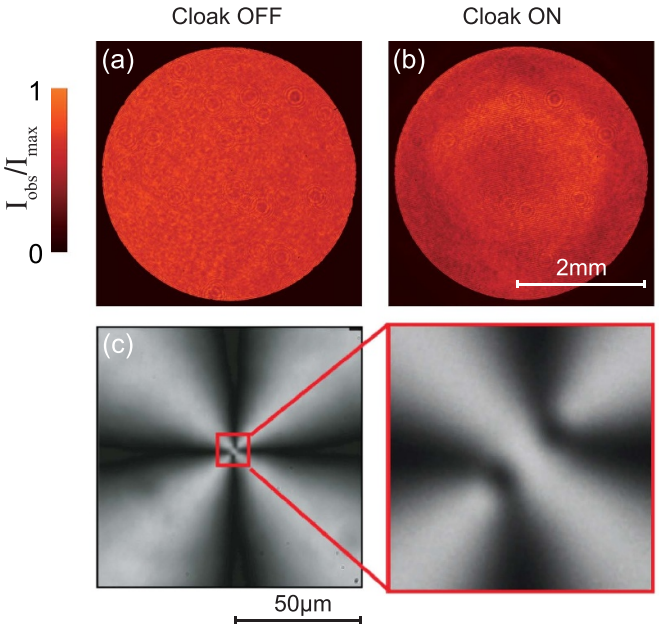

Figure 6. (a), (b) Normalized intensity distribution in the observation plane in the absence of the object when the cloak is deactivated (panel (a)) and activated (panel (b)). (c) Crossed linear polarizers imaging of the central part of the geometric phase mask with $m = 1$.

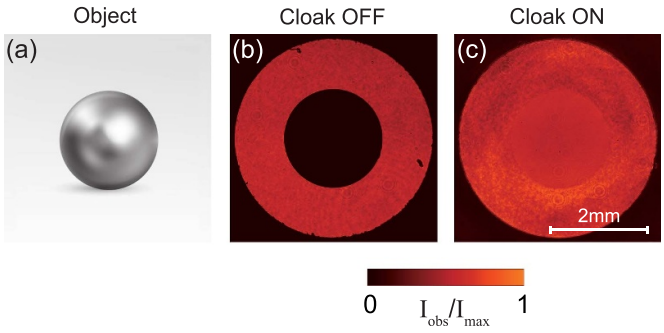

Figure 7. (a) Picture of the stainless steel sphere with radius $R_o = 1$ mm used as the object to conceal. (b), (c) Experimental observations at $\tilde{z} = 4$ in presence of the object placed in the center of the cloaking region $(r_o, z_o) = (0, 0)$ when the cloak is deactivated (panel (b)) and activated (panel (c)).

representative set of intensity distribution in the transverse plane is shown in figure 5, which can be compared to the numerical experiments reported in figures 1(d)–(f). A 3D reconstruction of the quasi-nodal cloaking volume with tube-like boundaries is reconstructed from a collection of several tens of intensity cross-sections images using Mayavi tool [28]. We also observe the re-imaged aperture at $\tilde{z} = 4$ without the object when the cloak is deactivated and activated, see figures 6(a) and (b), respectively. Non-uniform intensity distribution becomes clearly visible when the geometric phase masks are inserted in the optical system. This is quantitatively ascertained from the ratio between the standard deviation and the mean value of the intensity distribution for $r < R$, which increases by a factor of two as the vortex masks are inserted, from ∼0.085 to ∼0.16. We ascribe such a behavior to instrumental limitations such as the relative placement of the optical elements and the lack of resolution of structured birefringent masks, whose central part suffers from broken axisymmetric distribution of the optical axis, as illustrated in figure 6(c).

Then, we select a 2 mm diameter stainless steel metallic sphere for the cloaking demonstration, as shown in figure 7(a). The object is placed at $(r_o, z_o) = (0, 0)$ and its cloaking is reported in figures 7(b) and (c). These experimental results validate the numerical simulations shown in figures 2(b) and (d). The robustness of the optical cloak is highlighted by displacing the sphere along and perpendicular to the optical axis, as summarized in figures 8 and 9, which validate their numerical counterparts, figures 3 and 4.

Finally, the quantitative analysis of the cloaking performance is made by evaluating the Pearson correlation coefficient C between the recorded images in the observation plane when

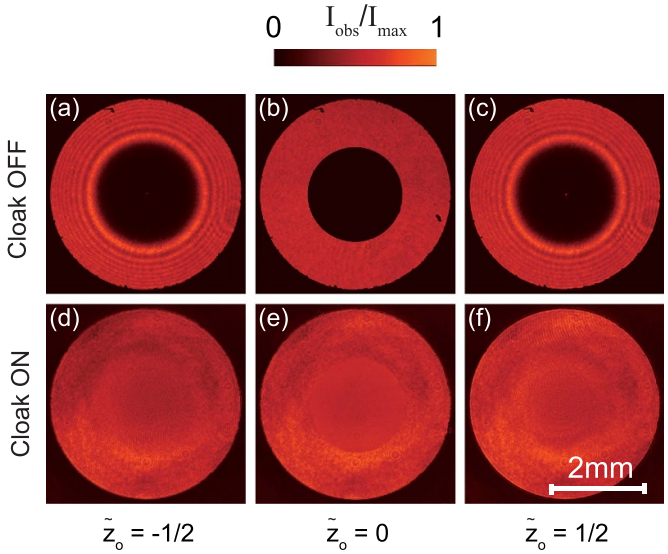

Figure 8. Experimental cloaking robustness versus the position of the object along the optical axis. Normalized intensity imaging in the observation plane when the cloak is deactivated (panels (a)–(c)) and activated (panels (d)–(f)) for $\tilde{z}_o = -0.5$ (first column), $\tilde{z}_o = 0$ (second column) and $\tilde{z}_o = 0.5$ (third column).

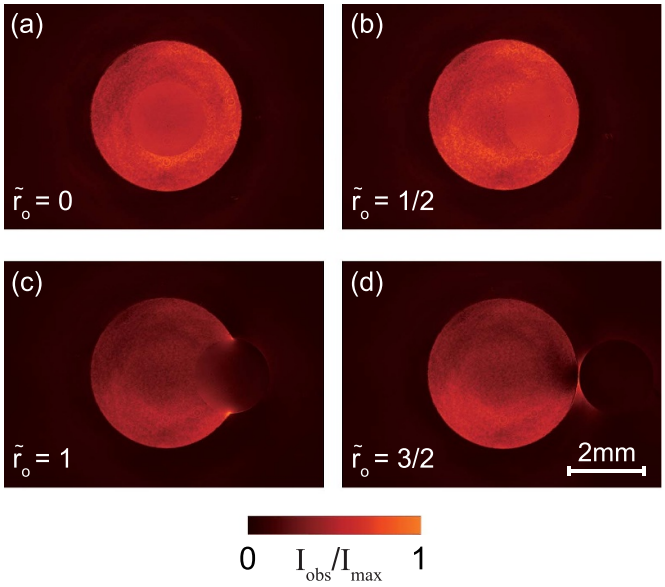

Figure 9. Experimental cloaking robustness versus the position of the object perpendicular to the optical axis. Normalized intensity imaging in the observation plane at $z_o = 0$ for $\tilde{r}_o = 0$ (a), $\tilde{r}_o = 0.5$ (b), $\tilde{r}_o = 1$ (c) and $\tilde{r}_o = 1.5$ (d).

the cloak is activated with and without the object. The dependence of C as a function of the on-axis position $\tilde{z}_o$ of the object is plotted in figure 10 for three different apertures with radii $R = 1.5$, 2 and 2.5 mm, for which we find $C = 0.91 \pm 0.05$, $C = 0.92 \pm 0.1$ and $C = 0.92 \pm 0.1$, respectively, whereas $C \simeq (0.46, 0.59, 0.70)$ when the cloak is deactivated.

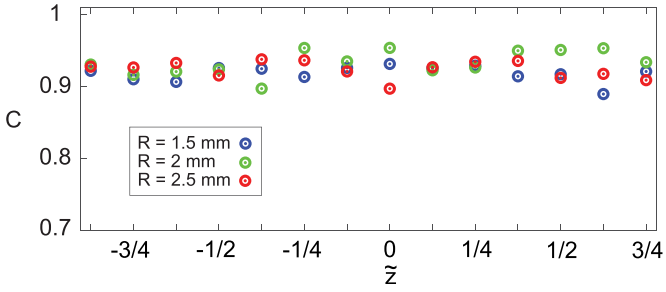

Figure 10. Dependence of the Pearson correlation coefficient C versus $\tilde{z}_o$ at $\tilde{r}_o = 0$ for three different apertures A with radius $R = 1.5$ mm (blue), 2 mm (green) and 2.5 mm (red).

5. Conclusion

A wave-optics approach to optical cloaking based on a quasi-nodal volume shaped from optical vortex Fourier filtering has been proposed, which is based on the use of a pair of pure phase masks imparting optical phase singularities with topological charge ± 2 to the light field. Numerical analysis and experimental demonstration have been reported in the framework of the concealment of macroscopic objects in the visible domain. The proposed approach is polarization independent and can be extended to any operating wavelength by using appropriate vortex beam shapers. In particular, the use of geometric phase vortex masks instead of dynamical phase ones provide enhanced polychromatic robustness, however at the expense of transmission losses and polarization-optics add-on when considering ultra-broadband fields.

Although the present work deals with axisymmetric cloaking regions, its extension to non-axisymmetric situation can be considered by using computer-assisted design toward the fabrication of appropriate singular phase masks [29]. Furthermore, we note that the generation of a nodal surface is not limited to the use of vortex phase masks of topological charge two but extends to all even charges [25], which opens for exploring the generalization of the present work to high-order vortex masks.

Data availability statement

The data that support the findings of this study are available upon reasonable request from the authors.

Funding

E B acknowledges funding from Conseil Régional de Nouvelle Aquitaine (Project HELIXOPTICS). M R and H M acknowledge funding from Science Committee of Armenia under the Grant Agreement No. 21T-1C331.

References

[1] Leonhardt U 2006 *Science* **312** 1777–80
[2] Pendry J B, Schurig D and Smith D R 2006 *Science* **312** 1780–2
[3] Alù A and Engheta N 2005 *Phys. Rev.* E **72** 016623
[4] Ward A and Pendry J B 1996 *J. Mod. Opt.* **43** 773–93
[5] McCall M *et al* 2018 *J. Opt.* **20** 063001
[6] Schurig D, Mock J J, Justice B, Cummer S A, Pendry J B, Starr A F and Smith D R 2006 *Science* **314** 977–80
[7] Li J and Pendry J B 2008 *Phys. Rev. Lett.* **101** 203901
[8] Chen H, Chan C T and Sheng P 2010 *Nat. Mater.* **9** 387–96
[9] Valentine J, Li J, Zentgraf T, Bartal G and Zhang X 2009 *Nat. Mater.* **8** 568–71
[10] Liu R, Ji C, Mock J, Chin J, Cui T and Smith D 2009 *Science* **323** 366–9
[11] Kundtz N and Smith D R 2010 *Nat. Mater.* **9** 129–32
[12] Ergin T, Stenger N, Brenner P, Pendry J B and Wegener M 2010 *Science* **328** 337–9
[13] Zhang S, Xia C and Fang N 2011 *Phys. Rev. Lett.* **106** 024301
[14] Chen X, Luo Y, Zhang J, Jiang K, Pendry J B and Zhang S 2011 *Nat. Commun.* **2** 1–6
[15] Gu C, Xu Y, Li S, Lu W, Li J, Chen H and Hou B 2015 *Sci. Rep.* **5** 1–7
[16] Jung J, Park H, Park J, Chang T and Shin J 2020 *Nanophotonics* **9** 3165–96
[17] Fan R H, Xiong B, Peng R W and Wang M 2020 *Adv. Mater.* **32** 1904646
[18] Xu H X, Hu G, Wang Y, Wang C, Wang M, Wang S, Huang Y, Genevet P, Huang W and Qiu C W 2021 *Light: Sci. Appl.* **10** 1–13
[19] Choi J S and Howell J C 2014 *Opt. Express* **22** 29465–78
[20] Zhang B, Luo Y, Liu X and Barbastathis G 2011 *Phys. Rev. Lett.* **106** 033901
[21] Howell J C and Howell J B 2013 arXiv:1306.0863
[22] Babayiğit C, Evren A S, Bor E, Kurt H and Turduev M 2019 *Phys. Rev.* A **99** 043831
[23] Zhao L and Yu M 2020 *Sci. Rep.* **10** 1–9
[24] Sun J, Zeng J, Wang X, Cartwright A N and Litchinitser N M 2014 *Sci. Rep.* **4** 1–4
[25] Mawet D, Riaud P, Absil O and Surdej J 2005 *Astrophys. J.* **633** 1191
[26] Foo G, Palacios D M and Swartzlander G A 2005 *Opt. Lett.* **30** 3308–10
[27] Collins S 1970 *J. Opt. Soc. Am.* **60** 1168–77
[28] Mayavi is a general purpose, cross-platform tool for 2D and 3D scientific data visualization in Python. The code used to obtain figure 5(d) can be found at https://github.com/photonics-ai-lab/Three-dimensional-construction-of-the-ring-of-fire-diffraction-by-Mayavi
[29] Ruane G J, Swartzlander G A, Slussarenko S, Marrucci L and Dennis M R 2015 *Optica* **2** 147–50